THE JOURNAL OF PHYSICAL CHEMISTRY C

Article

Cite This: J. Phys. Chem. C 2018, 122, 177−184

pubs.acs.org/JPCC

Enhancing Ferroelectric Dipole Ordering in Organic−Inorganic Hybrid Perovskite $CH_3NH_3PbI_3$: Strain and Doping Engineering

Yuheng Li, Maziar Behtash, Joseph Wong, and Kesong Yang*

Department of NanoEngineering, University of California San Diego, 9500 Gilman Drive, Mail Code 0448, La Jolla, California 92093-0448, United States

ABSTRACT: Organic−inorganic hybrid perovskites with a prototype formula $MAPbI_3$ ($MA = CH_3NH_3$) have shown great promise in next-generation solar cells, yet a full understanding of their high power conversion efficiency relative to their inorganic counterparts has not been achieved. One of the most plausible arguments for their high efficiency is the ability of organic cations to form ferroelectric (FE) domains. By using first-principles calculations to examine the rotational behavior of MA cations in $MAPbI_3$, here we show a relationship between the lattice structures and the FE dipole ordering of MA cations. It is found that the MA cations could form a spontaneous FE dipole ordering in tetragonal $MAPbI_3$ at room temperature. The tendency of the FE formation is strongly related to the ratio of lattice parameters of $MAPbI_3$. On the basis of the developed structure−ferroelectric-property relationship, we propose that a biaxial or uniaxial compressive strain and an anion doping with small halogen ions can further enhance the FE dipole ordering. These findings are in good agreement with the experimental discoveries that high-performance solar cells always incorporate mixed halide hybrid perovskites involving Br or Cl ions. This work may provide some guidelines for rational designs of highly efficient hybrid perovskite solar cells.

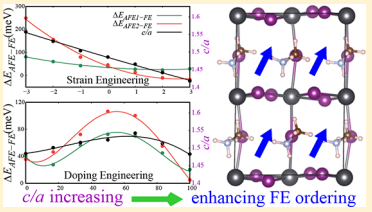

INTRODUCTION

Organic−inorganic hybrid perovskites have gained considerable attention in recent years because of their exceptional properties for next-generation photovoltaic applications.[1,2] Solar cells employing hybrid perovskites have shown an unprecedented rise in power conversion efficiency and have reached a recent record efficiency of 22.1%.[3] The high power conversion efficiency is largely attributed to the intrinsic optoelectronic properties of hybrid perovskites,[4−8] such as an appropriate band gap matched with the visible-light solar spectrum,[9,10] high optical absorption,[11] small electron and hole effective masses,[12] long carrier diffusion length,[13−17] and the possible existence of ferroelectric (FE) domains.[18] In addition, their low-temperature solution processability makes them substantially cost-effective for large-scale applications.[19,20]

In spite of promising photovoltaic applications of hybrid perovskites, the origin of the high power conversion efficiency, particularly the role of organic cations, is still an open question.[21−23] Recent studies have indicated that the superior performance of hybrid perovskites with respect to that of their inorganic counterparts is derived from the organic cations.[21,24−29] One of the most prevalent arguments is that intrinsic dipoles of the organic cations are likely to form nanoscale FE domains, which are thought to play a critical role in the efficient separation of photoinduced electron−hole pairs that leads to the high power conversion efficiency.[24−26,28,29] Nevertheless, the movement and ordering of organic cations are still controversial in both theoretical[24,30−32] and experimental studies,[18,26,33−36] and far from a complete understanding.

From a theoretical perspective, the polarization intensity contributed from the organic cations is particularly controversial. Walsh et al.'s first-principles calculations indicate a spontaneous formation of FE domains in $MAPbI_3$ and a large polarization value of 38 $\mu C/cm^2$.[24] A later first-principles computational study showed that MA cations in tetragonal $MAPbI_3$ have a preferential alignment along the *c*-axis, and the polarization intensity is estimated to be 4.42 $\mu C/cm^2$, which is mainly contributed by the MA dipole.[30] The authors also explained that the large discrepancy from Walsh's study was possibly due to the neglect of the relaxations or the possible inclusion of polarization quanta. Rappe et al. reported that the bulk polarization contribution solely from the organic molecular dipole moment is less than 2.5 $\mu C/cm^2$, and the PbI_3 inorganic lattice has a major contribution to the polarization.[31] Moreover, their calculations showed that the antiferroelectric (AFE) tetragonal structure with nearly zero net polarization is more stable than its FE counterpart by 21 meV, implying that the FE domains cannot form spontaneously at room temperature. On the other hand, Wang et al. used first-principles electronic structure calculations to reveal an FE tetragonal structure with a polarization of about 8 $\mu C/cm^2$, primarily contributed by the organic cations.[32]

From an experimental perspective, there has been a direct observation of FE domains in high-quality β-$MAPbI_3$ perovskites using piezoforce microscopy.[18] A later experimental study reported the FE polarization behavior in the $MAPbI_3$ perovskite crystal and confirmed the formation of spontaneous polarization even without the presence of an electric field.[33] A ferroelectric hysteresis and polar domains in tetragonal $MAPbI_3$ were also observed through dielectric response and chemical etching, respectively.[26] On the contrary, Weller et al. investigated the full structure of $MAPbI_3$ using neutron powder

Received: October 20, 2017
Revised: December 12, 2017
Published: December 12, 2017

DOI: 10.1021/acs.jpcc.7b10413
J. Phys. Chem. C 2018, 122, 177−184

diffraction and found that the cations were disordered in the tetragonal phase,[34] implying no polarization. Sharada et al. claimed a nonpolar or centrosymmetric structure of $MAPbI_3$ using a time-resolved pump−probe measurement of the second-harmonic generation efficiency.[35] Similarly, in the case of $MAPbBr_3$, it was found that the compound is centrosymmetric and nonpolar and thus could not be ferroelectric by using a second-harmonic generation spectroscopy.[36] All these irreconcilable experimental results indicate that a more comprehensive computational and theoretical study is essential to understand whether the organic cations can form a ferroelectric dipole ordering and to further elucidate the roles of organic cations in the hybrid perovskite solar cells.

In this work, we explore ferroelectric dipole ordering in $MAPbI_3$ using first-principles calculations. This article is organized as follows. First, we discuss two types of rotation modes of MA cations: in-phase rotation and out-of-phase rotation. Next, we explore the possibility of spontaneous formation of FE dipole ordering in tetragonal $MAPbI_3$. Finally, we propose two nanoengineering approaches to further enhance the FE dipole ordering, i.e., strain engineering and doping engineering.

COMPUTATIONAL DETAILS

First-principles density functional theory (DFT) calculations were performed using the Vienna ab Initio Simulation Package (VASP).[37,38] The Projector Augmented Wave (PAW) pseudopotential was used for describing electron−ion interactions,[39] and the Generalized Gradient Approximation (GGA) parametrized by Perdew−Burke−Ernzerhof (PBE) was used for treating electron−electron exchange-correlation functional.[40] A cutoff energy of 400 eV for the plane-wave basis set was used, and Γ-centered 6 × 6 × 6 and 4 × 4 × 2 k-point meshes were used for cubic and tetragonal structures, respectively. Lattice parameters and atomic positions were optimized until all components of the residual forces were smaller than 0.01 eV/Å, and the convergence threshold for self-consistent-field iteration was set at 10^{-5} eV.

RESULTS AND DISCUSSION

In-Phase Rotation. We begin by studying the in-phase rotational behavior of MA cations in cubic and tetragonal $MAPbI_3$ phases, respectively. Here, an in-phase rotation refers to a rotation of all the MA cations in synchrony. In this work, the experimental lattice parameters of a = 6.31 Å for the cubic phase[41] and a = 8.80 Å, c = 12.99 Å for the tetragonal phase[42] were used. The calculated dipole moment of a single MA cation is about 2.38 D, with a direction from N to C, which is consistent with previously reported values of 2.29 D.[24] It is noted that, in principle, there are numerous in-phase rotation modes for the MA cations in $MAPbI_3$. To simplify the computational models, we consider two types of in-phase rotation modes: (i) MA cations rotate around their C−N axes and keep their dipole direction fixed (nonflipping mode), and (ii) MA cations rotate around their centers and flip their dipole direction (flipping mode). To explore the MA rotational behaviors, we calculated the total energy changes (ΔE) as a function of the rotation angles of MA cations (Figure 1). For the nonflipping mode, considering the C_{3v} symmetry of the MA cation, we performed total energy calculations for each structure with MA rotation in discrete steps ranging from 0 to 120° (see Figure 1a for cubic phase and Figure 1c for tetragonal phase). For the flipping mode, the rotation range of the MA is from 0 to 180° (Figure 1b and Figure 1d). Our calculations reveal the following two conclusions:

(1) For the nonflipping rotation mode (Figure 1a and 1c), ΔE shows similar dependence on θ in the cubic and tetragonal phases. In each case, the rotation energy barrier is smaller than 5 meV (Figure 1a′ and 1c′), indicating that the nonflipping rotation mode is accessible in both phases. The energy barrier in the cubic phase is slightly lower than that in the tetragonal phase (2 versus 4 meV), which is due to a more spacious framework around the MA cation in the cubic phase structure. Interestingly, the rotation has a period of 90° in both the cubic and tetragonal phases, which is due to the quadrangle environment of the inorganic frameworks.

(2) For the flipping rotation mode (Figure 1b and 1d), the rotation energy barrier is about 6 meV in the cubic phase and 160 meV in the tetragonal phase (Figure 1b′ and 1d′), indicating that the flipping rotation mode is accessible in the cubic phase but energetically prohibited in the tetragonal phase. Moreover, the calculated value of ΔE versus θ for the tetragonal phase shows a deep trough around 50°, indicating that MA cations tend to stay at an orientation of around 50° with respect to the c-axis in the tetragonal phase.

Next, we analyze the origin of the different energy barriers of flipping rotation in cubic (Figure 1b) and tetragonal (Figure 1d) phases from the perspective of cell geometry. The tetragonal $MAPbI_3$ unit cell can be considered as consisting of four subunit cells, each of which contains one MA cation (Figure 1d). The lattice parameters of each subunit cell can be calculated from those of the $MAPbI_3$ unit cell using the equations: $a' = a/\sqrt{2} = 8.80/\sqrt{2} = 6.22$ Å and $c' = c/2 = 12.99/2 = 6.50$ Å. This subunit cell is more slender than the cubic unit cell with lattice constant a = 6.31 Å (Figure 1b). In other words, each subunit cell in the tetragonal phase has a shorter bottom edge (a') but longer vertical edge (c') than the cubic unit cell, like experiencing a compressive strain in the bottom plane. As a result, as the C−N bond of the MA cation rotates closer to an orientation parallel to the bottom plane, the MA cation tends to undergo greater steric repulsive forces from the inorganic framework, thus leading to the higher energy barrier. On the basis of this analysis, we can infer a general rule regarding the flipping rotation of MA cations: the larger the cell aspect ratio (c/a) is, the less likely MA flipping rotation becomes. As discussed later, this general rule will be applied to enhance the ferroelectric dipole ordering of MA cations.

Out-of-Phase Rotation. In the tetragonal $MAPbI_3$ unit cell, in addition to the in-phase flipping rotation, there is also out-of-phase flipping rotation that refers to a rotation of MA cations out of synchrony. For a dipole ordering study, an out-of-phase rotation model can be simplified such that only two out of the total four MA cations rotate. In other words, a pair of MA cations in the $MAPbI_3$ unit cell rotate, while the other pair of MA cations are fixed. The difference between in-phase and out-of-phase rotations can be explained as below. For in-phase rotation, dipoles of all MA cations are always in alignment and form an FE state. For out-of-phase rotation, the relative angle between rotating and fixed MA cations is dynamic. When the angle reaches 180°, the dipoles of the rotating MA pair and the fixed MA pair completely cancel out and yield an AFE state with zero net polarization. A rotation process with the angle changing from 0° to 180° represents an FE-to-AFE transition.

DOI: 10.1021/acs.jpcc.7b10413
J. Phys. Chem. C 2018, 122, 177−184

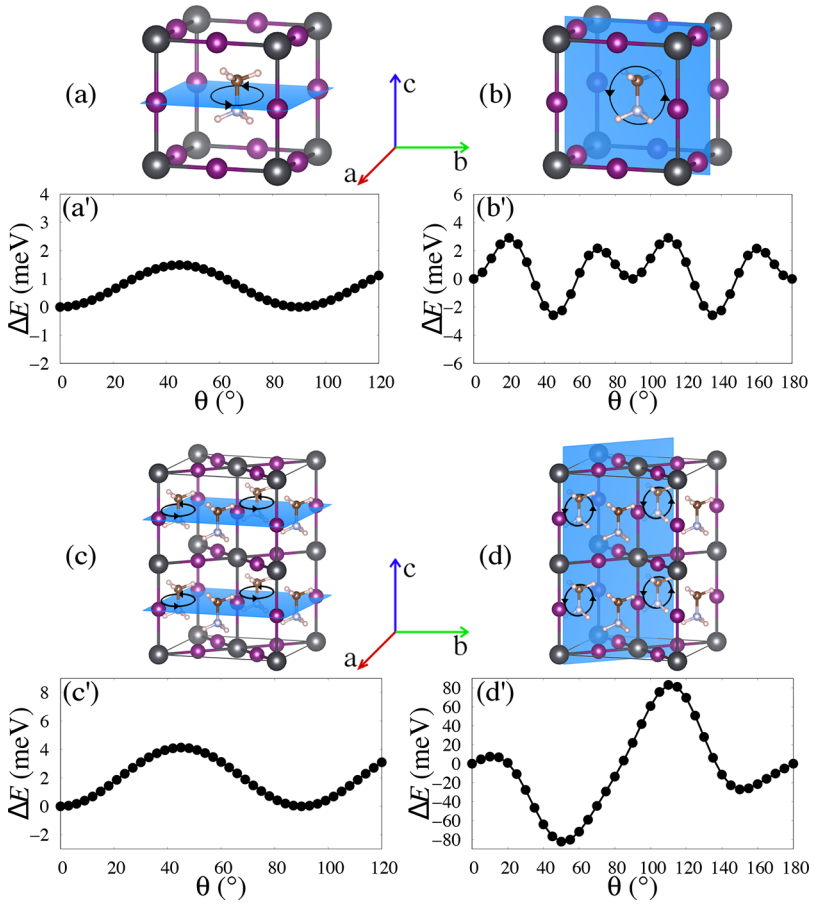

Figure 1. Scheme of the rotation modes for the MA cations (a–d) and corresponding total energy change (ΔE) as a function of the rotation angle (θ) (a′–d′). (a–d) show the MA rotation in (a) cubic (001) rotation plane, (b) cubic (100) rotation plane, (c) tetragonal (001) rotation plane, and (d) tetragonal (110) rotation plane. The blue shadows and the black arrows in the blue shadows illustrate the rotation planes and rotation directions of MA cations, respectively. The unit cells are shown in standard orientations of crystal shape using VESTA.[43]

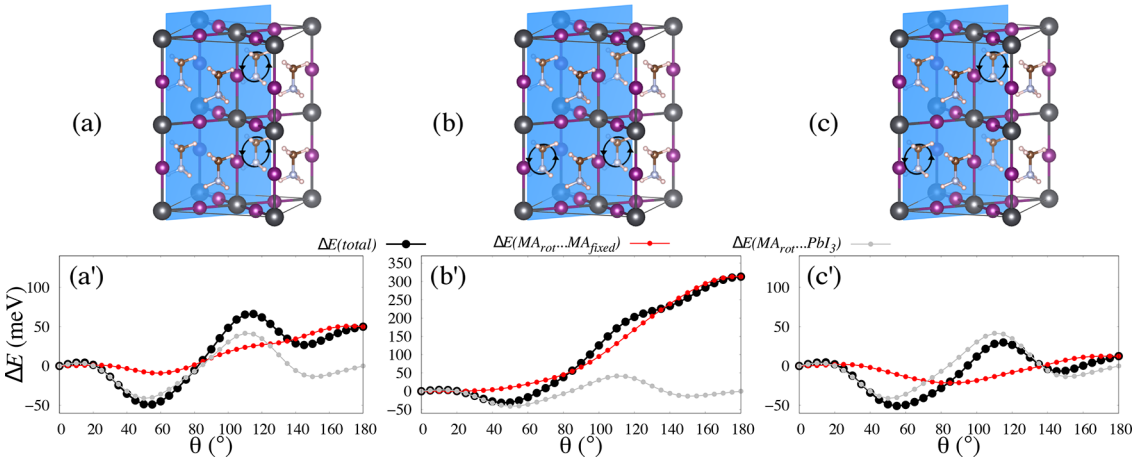

Figure 2. Calculated total energy change, ΔE(total), as a function of MA out-of-phase rotation angle, θ, in the tetragonal $MAPbI_3$: (a) FE to AFE1, (b) FE to AFE2, and (c) FE to AFE3. The initial state of the four MA cations is set as FE ordering, and as θ increases up to 180°, the final state becomes AFE (three AFE states are considered here, labeled as AFE1, AFE2, and AFE3, respectively). Black curves show the total energy change, labeled as ΔE(total). Red curves show the total energy change induced by interaction between rotating and fixed MA cations, labeled as $\Delta E(MA_{rot}\cdots MA_{fixed})$. Gray curves show the total energy change induced by interaction between rotating MA cations and the PbI_3 inorganic framework, labeled as $\Delta E(MA_{rot}\cdots PbI_3)$.

The two rotating MA cations can be in the same column (Figure 2a), in the same row (Figure 2b), or in the same diagonal (Figure 2c), and their (110) rotation plane is highlighted in blue. Their corresponding AFE states are labeled as AFE1, AFE2, and AFE3, respectively. To study whether these FE-to-AFE transitions are energetically accessible, we calculated total energy changes for out-of-phase rotation models, from the FE state to the three AFE states. In our calculations, to clearly

DOI: 10.1021/acs.jpcc.7b10413
J. Phys. Chem. C 2018, 122, 177–184

show the pure contribution of MA rotation to the total energy change, the PbI_3 inorganic framework is unrelaxed. The total energy changes during these FE-to-AFE transitions are shown in Figures 2a′, 2b′, and 2c′. Notably, the total energy change, ΔE(total), in an out-of-phase rotation model comes from two parts: (1) the interaction between rotating MA cations and PbI_3 inorganic framework and (2) the interaction between rotating and fixed MA cations. The total energy changes induced by these two interactions are labeled as $\Delta E(MA_{rot}\cdots PbI_3)$ and $\Delta E(MA_{rot}\cdots MA_{fixed})$, respectively. As a result, we have the following equation.

$$\Delta E(\text{total}) = \Delta E(MA_{rot}\cdots PbI_3) + \Delta E(MA_{rot}\cdots MA_{fixed}) \quad (1)$$

The total energy change in the out-of-phase rotations is different from that in the in-phase rotations because the latter comes exclusively from the interaction between the rotating MA cations and PbI_3 inorganic framework. To clearly show the contribution of interaction between rotating and fixed MA cations in the FE-to-AFE transitions, we calculated $\Delta E(MA_{rot}\cdots MA_{fixed})$ from eq 1. In this equation, $\Delta E(MA_{rot}\cdots PbI_3)$ is half the value of the energy change in the in-phase rotation mode (Figure 1d). This is because the $\Delta E(MA_{rot}\cdots PbI_3)$ here is induced by the interaction between PbI_3 and only two rotating MA cations, instead of four rotating MA cations in the in-phase rotation mode. The calculated ΔE(total), $\Delta E(MA_{rot}\cdots PbI_3)$, and $\Delta E(MA_{rot}\cdots MA_{fixed})$ are plotted in Figure 2 as black, gray, and red curves, respectively. From these results, we can get the following conclusions.

(1) ΔE(total) (black curves in Figure 2), has barriers of about 120, 320, and 80 meV for transitions from the FE state to AFE1, AFE2, and AFE3 states, respectively. These barriers are far above kT at room temperature (26 meV), indicating that all the three FE-to-AFE transitions are energetically prohibited. For each case, there is an energy trough around 50° and an energy peak around 110°. This trough−peak pattern is similar to that of $\Delta E(MA_{rot}\cdots PbI_3)$ (gray curves in Figure 2), indicating that the pattern is mainly caused by interaction between rotating MA cations and the PbI_3 inorganic framework.

(2) $\Delta E(MA_{rot}\cdots MA_{fixed})$ has energy barriers of about 60, 300, and 30 meV for transitions from the FE state to AFE1, AFE2, and AFE3 states, respectively (red curves in Figure 2). These barriers are above kT as well, although they are solely induced by the interaction between rotating and fixed MA cations. This provides more direct evidence that the FE-to-AFE transitions are inaccessible at room temperature. The trough−peak pattern of ΔE(total) and $\Delta E(MA_{rot}\cdots PbI_3)$ is absent in $\Delta E(MA_{rot}\cdots MA_{fixed})$, indicating that this pattern is irrelevant to the interaction between rotating and fixed MA cations. Specifically, for the FE-to-AFE1 and FE-to-AFE3 transitions, they have a shallow trough around 60° (Figure 2a′) and 85° (Figure 2c′), respectively. Each of these angles represents an energetically favored direction of the corresponding rotating MA pair. This indicates that, in these two out-of-phase rotations, the rotating and fixed MA pairs are not in a perfect alignment at their ground states, but they can still yield a nonzero net FE polarization. For the FE-to-AFE2 transition, the red curve shows a monotonic increase in energy from 0° to 180° (Figure 2b′). This indicates that, in this out-of-phase rotation, the rotating MA pair tends to stay at 0°, forming a FE dipole ordering with the still MA pair. In short, the out-of-phase MA rotations which result in an FE-to-AFE transition are energetically prohibited. For all the three out-of-phase rotations, MA cations in tetragonal $MAPbI_3$ tend to form the FE state with nonzero net polarization.

Spontaneous Ferroelectric Dipole Ordering. The preceding results based on the unrelaxed tetragonal $MAPbI_3$ lattice show that the MA cations tend to form an FE state. In reality, however, the structural distortion of PbI_3 could significantly affect the total energy of this material and the MA orientations. Hence, to accurately determine MA orientation, cell geometry, and energetic advantage of the FE state, we also carried out total energy calculations for fully relaxed structures with MA cations in all the FE and AFE states. This procedure involves two steps. First, on the basis of a relaxed FE structure, we produced three AFE structures by exchanging C and N atoms in the two corresponding MA cations and then fully relaxed all these structures. Their optimized lattice parameters are listed in Table 1, along with the experimental values.

Table 1. Relaxed Lattice Parameters of the $MAPbI_3$ with Different MA Ordering Configurations and Their Discrepancies (δ) with the Experimental Values

phase	a (Å)	b (Å)	c (Å)	α (deg)	β (deg)	γ (deg)	δ (%)
expr[8]	8.85	8.85	12.64	90.00	90.00	90.00	–
FE	8.78	8.79	13.04	89.20	89.09	89.56	1.17
AFE1	8.80	8.80	13.04	88.62	88.55	89.82	1.27
AFE2	8.76	8.98	12.85	87.92	87.18	89.96	1.61
AFE3	8.93	8.91	12.70	86.99	87.09	89.23	1.58

To determine which structure among the four states is closest to the experiment, we define *lattice discrepancy* (δ) using following equation

$$\delta = \frac{1}{6}\Sigma\frac{|p - p_{expr}|}{p_{expr}} \quad (2)$$

in which p represents the six lattice parameters. The calculated δ values of the four states are listed in Table 1. Our results show that the optimized lattice parameters of the FE state have the smallest δ of 1.17%, indicating that this set of lattice parameters is closest to the experimental values.

Next, we took the lattice parameters of the FE state as a standard for best simulating actual case. The three AFE states were modeled again by manually exchanging corresponding C and N atoms in the fully relaxed FE structure. All the atomic positions of the FE and three AFE structures were relaxed with their lattice parameters fixed. This procedure ensures us to accurately produce the energy difference between AFE and FE states. All the optimized structures are shown in Figure 3.

After structural optimization, the MA cations tend to keep their original configurations in all the FE and AFE structures. MA cations with their dipoles pointing up are highlighted in blue, while those with their dipoles pointing down are highlighted in green (Figure 3). In the FE structure, all four MA cations point up along the [111] direction (Figure 3a). In the AFE structures, two MA cations point up and the other two point down, yielding a polarization of zero (Figure 3b, 3c, and 3d). It is also found that there is a distortion in the PbI_3 inorganic framework for all four optimized structures and that AFE3 has the most severe distortion. Our results show that FE is the most stable state and is

DOI: 10.1021/acs.jpcc.7b10413
J. Phys. Chem. C 2018, 122, 177−184

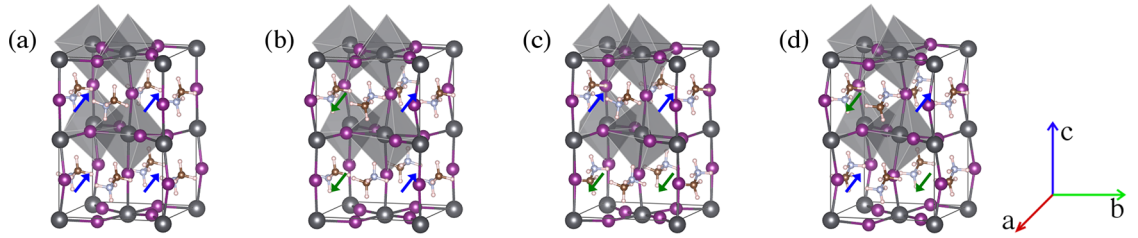

Figure 3. Relaxed structures with different MA ordering configurations: (a) FE, (b) AFE1, (c) AFE2, and (d) AFE3. Blue arrows show MA dipoles pointing up, and green arrows show MA dipoles pointing down.

energetically more favorable than the three AFE states by 40, 36, and 65 meV, respectively. These results indicate that tetragonal $MAPbI_3$ is inclined to form the FE state and has a net polarization from ferroelectric dipole ordering. However, the energy difference between the most stable AFE state and the FE state is only about 36 meV, close to kT (26 meV) at room temperature. This indicates that the FE state's energetic advantage is relatively small and thus that AFE states might be accessible with slight thermal fluctuations at ambient conditions. In other words, the weak inclination of FE state can be readily eliminated, and the FE characteristics can fall below the experimental detection limit. This could be a reason why some previous experimental studies showed no ferroelectricity.[32,35]

It is noted that the structures in our calculations represent ideal configurations with MA either completely in phase (FE) or completely out of phase (AFE) with respect to their neighbors. In reality, a wide range of possible structures exists between these two extreme cases, although these ideal FE and AFE models can give a direct indication of ferroelectric dipole ordering. Our results are consistent with a previous theoretical study[30] in which they proved a preferential MA alignment in tetragonal $MAPbI_3$ through comparing the energy of three intermediate configurations. In addition, by using the calculated dipole moment of 2.38 D for a single MA cation, we calculated the polarization value of tetragonal $MAPbI_3$ contributed by MA's intrinsic dipole moment and determined a value of 3.15 $\mu C/cm^2$. This value is close to previous results of 4.42 $\mu C/cm^2$[30] and 8 $\mu C/cm^2$.[32] Both of these results show that the main contribution to the overall polarization is the dipole alignment of MA cations rather than the distortion of the PbI_3 inorganic framework.

Strain Engineering. As discussed earlier, the MA flipping rotation is strongly related to cell aspect ratio (c/a) of $MAPbI_3$. As c/a becomes larger, the MA flipping rotation becomes energetically less likely, implying a larger energy difference between an AFE state and FE state (this energy difference is defined as ΔE_{AFE-FE}). On the basis of this finding, one might expect that a compressive biaxial or uniaxial strain can enlarge c/a of tetragonal $MAPbI_3$[44,45] and enhance the FE state's energetic advantage over the AFE states. To verify this hypothesis, we calculated ΔE_{AFE-FE} and c/a with respect to biaxial strain and uniaxial strain from −3% to +3%, with negative (positive) values defined as compressive (tensile) strain. As discussed earlier, the AFE3 configuration has a very high energy and severe distortion, and we therefore exclude this configuration in our following discussion. In our calculations, lattice parameters in ab-plane are fixed, while c and all the atomic positions are fully relaxed.

The calculated energy difference between AFE1 (AFE2) and the FE state is shown in green (red) in Figure 4, labeled as $\Delta E_{AFE1-FE}$ ($\Delta E_{AFE2-FE}$). The calculated c/a is shown in black

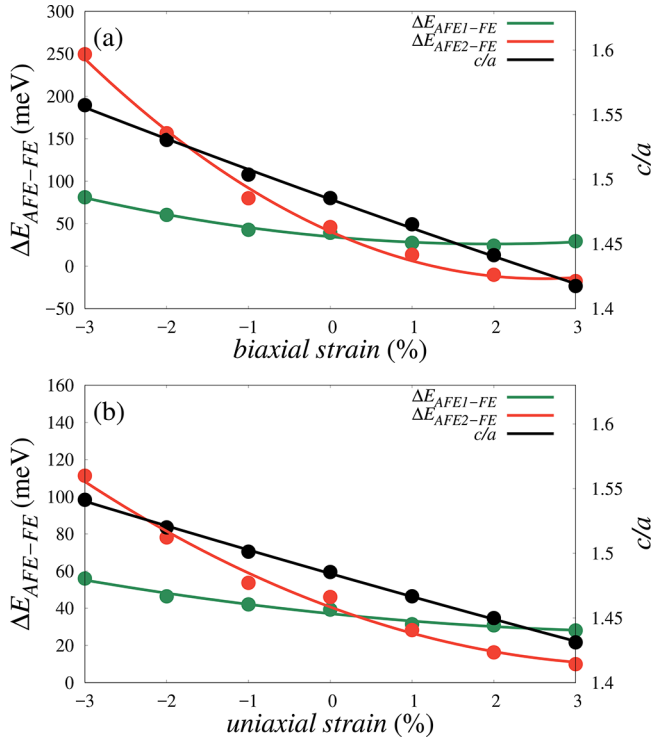

Figure 4. Energy difference between each AFE structure and the FE structure (ΔE_{AFE-FE}) and cell aspect ratio (c/a) versus (a) biaxial strain and (b) uniaxial strain.

for structural analysis. Note that the c/a values are extracted from the FE state, because FE and AFE states under the same strain have negligible differences in c after optimization. Our calculations reveal the following conclusions.

(1) For both biaxial strain and uniaxial strain cases, ΔE_{AFE-FE} generally decreases from compressive strain to tensile strain, and $\Delta E_{AFE2-FE}$ decreases faster than $\Delta E_{AFE1-FE}$. Under compressive strains (from −3% to 0%), the AFE1 state is energetically more favorable than the AFE2 state, and $\Delta E_{AFE1-FE}$ can be as large as 81 meV (for biaxial strain) or 56 meV (for uniaxial strain), implying robust ferroelectric dipole orderings. Under tensile strains (from 0% to +3%), the AFE2 state has a lower total energy, and $\Delta E_{AFE2-FE}$ can be lower than −15 meV for biaxial strain or close to zero for uniaxial strain, implying paraelectric dipole orderings.

(2) The aspect ratio c/a also decreases from compressive strain to tensile strain, showing a strong correlation with ΔE_{AFE-FE} for both biaxial strain and uniaxial strain cases. As a and b decrease under biaxial compressive strain (as a decreases under uniaxial compressive strain), c and c/a always increase. The consequent larger c/a, as

DOI: 10.1021/acs.jpcc.7b10413
J. Phys. Chem. C 2018, 122, 177−184

indicated earlier, makes MA flipping rotation more difficult. As expected, the FE state's energetic advantage over the AFE states is enhanced based on the change of c/a.

In short, compressive biaxial or uniaxial strain increases the energetic advantage of the FE state over the AFE states, while tensile strain decreases it. Hence, strain engineering is one way to enhance the tendency of ferroelectric dipole ordering in tetragonal $MAPbI_3$.

Doping Engineering. In addition to strain engineering, herein we propose another way to enhance ferroelectric dipole ordering through doping engineering. That is, to substitute I with smaller halogen anions, such as Br or Cl. This hypothesis is based on the argument that substitutional doping with smaller ions exerts natural compressive strain on unit cells.[46,47] Moreover, doping can also induce lattice strains, which is much easier to achieve than through the application of external forces.[48] There are two kinds of I sites in tetragonal $MAPbI_3$: one on the PbI_2 layers, and the other on the MAI layers. Br (Cl) doping on the PbI_2 layers shortens Pb−halogen bonds in the ab-plane and reduces the a and b lattice parameters; while the doping on the MAI layers shortens Pb−halogen bonds along the c-axis and reduces the c lattice parameter. Therefore, in order to increase c/a, the ideal doping should be on the PbI_2 layers rather than the MAI layers. In fact, our calculations show that Br doping on the PbI_2 layers is energetically more favorable than that on the MAI layers by 16 meV. Additionally, there are eight I anions on the PbI_2 layers per unit cell while four on the MAI layers, implying that there is a higher probability for the doping to substitute I on the PbI_2 layers. These findings indicate that substitutional Br (Cl) anions prefer to go to the PbI_2 layers and are able to increase c/a. By taking Br-doped $MAPbI_3$ as an example, we calculated $\Delta E_{AFE1-FE}$, $\Delta E_{AFE2-FE}$, and c/a. These values are plotted with respect to doping concentration (c_{Br}) in Figure 5a. Our results indicate the following conclusions.

(1) The energy differences, $\Delta E_{AFE1-FE}$ and $\Delta E_{AFE2-FE}$, first increase and then decrease as c_{Br} increases, and they have a maximum value at $c_{Br} \approx 60\%$. At the peak, the AFE1 state has a lower total energy than the AFE2 state. The corresponding $\Delta E_{AFE1-FE}$ is as large as 75 meV, which means that the FE state can be stabilized at room temperature. At $c_{Br} > 60\%$, ΔE_{AFE-FE} decreases. At $c_{Br} = 100\%$, the compound becomes $MAPbBr_3$, and ΔE_{AFE-FE} has a minimum value of 4.88 meV, indicating that there is no spontaneous dipole alignment in pristine $MAPbBr_3$. In fact, a prior experimental study on $MAPbBr_3$ showed that $MAPbBr_3$ is centrosymmetric and nonpolar,[36] which is in excellent agreement with our results. Overall, in the wide doping concentration range, $30\% < c_{Br} < 80\%$, the FE state has a larger energetic advantage than the AFE states relative to the undoped $MAPbI_3$.

(2) The cell aspect ratio, c/a, has a similar trend as ΔE_{AFE-FE} and has a maximum value at $c_{Br} = 67\%$. This phenomenon can be explained as follows. The Br anions were first doped in the PbI_2 layers at $0\% \le c_{Br} \le 67\%$, which is similar to the case of ab-plane compressive strain. The Br doping in the PbI_2 layers leads to a reduction of the lattice parameters a and b and thus increases c/a. The increase in c/a enhances the relative stability of the FE state. At $c_{Br} > 67\%$, Br anions begin to substitute I anions in the MAI layers. The shortened Pb−halogen bonds along the c-axis decrease c/a. As c_{Br} increases up to 100%, c/a is eventually close to the value of pristine $MAPbBr_3$.

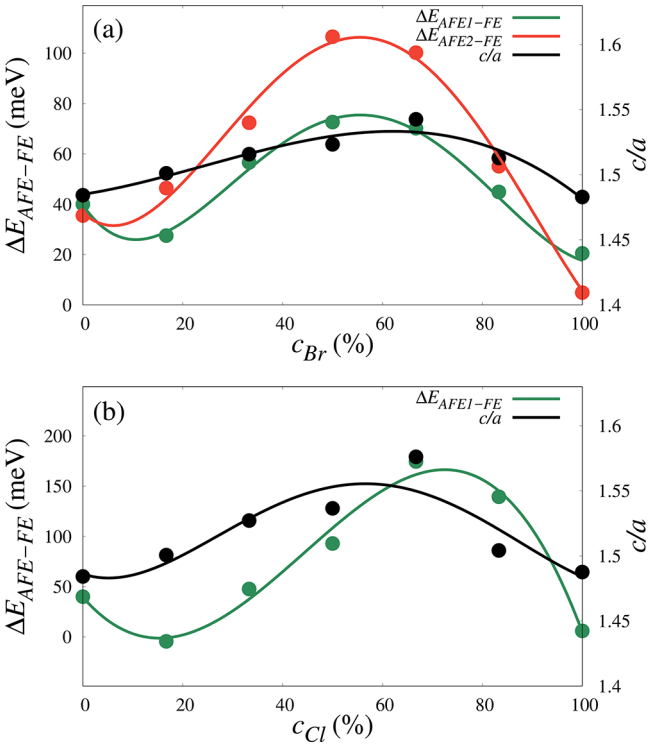

Figure 5. Energy difference between each AFE structure and the FE structure (ΔE_{AFE-FE}) and cell aspect ratio (c/a) versus (a) Br and (b) Cl doping concentrations, c_{Br} and c_{Cl}.

In other words, the similar trend of c/a and ΔE_{AFE-FE} implies that the doping engineering has a similar effect as the strain engineering.

Besides Br doping, we also calculated ΔE_{AFE-FE} and c/a for Cl doping with respect to doping concentration, c_{Cl}, as shown in Figure 5b. $\Delta E_{AFE1-FE}$ and c/a show a similar trend as in the case of Br doping. However, one notable difference from Br doping is that Cl doping induces more significant changes in c/a and ΔE_{AFE-FE}, which is attributed to the smaller size of Cl ions compared to Br ions. Moreover, because Cl ions are substantially smaller than I ions, Cl-doped $MAPbI_3$ structures exhibit severe structural distortion, particularly for the AFE2 configuration, which leads to unreasonably high $\Delta E_{AFE2-FE}$. Therefore, when evaluating the energetic preference of the FE state, only the $\Delta E_{AFE1-FE}$ is considered. In addition, it is noted that spin−orbit-coupling (SOC) plays an important role in determining the electronic structure in the Pb-based compounds.[45] To study whether the SOC will influence the energetic preference of ferroelectric dipole ordering, we have compared the ΔE_{AFE-FE} with SOC and without SOC and found that they exhibit nearly the same trend, indicating that the SOC has little effect on the dipole ordering.

In short, substitutional anion doping with smaller anions effectively enhances the tendency of FE dipole ordering in tetragonal $MAPbI_3$. In fact, prior studies have shown that Cl doping reduces charge recombination in lead iodide hybrid perovskites,[49,50] which supports our doping engineering results. Moreover, we expect that, by substitutional cation doping such as partially replacing MA with larger FA cations, the c-axis and c/a will also increase, and a similar effect of FE dipole ordering enhancement can also be achieved. Interestingly, this conclusion of dopant-mediated FE enhancement shows good agreement with the fact that high-performance solar cells always incorporate

DOI: 10.1021/acs.jpcc.7b10413
J. Phys. Chem. C 2018, 122, 177−184

mixed-halide hybrid perovskites such as $MAPbI_{3-x}Cl_x$, $MAPbI_{3-x}Br_x$, and $MA_{1-x}FA_xPbI_3$.[51−53]

CONCLUSION

In summary, ferroelectric dipole ordering of MA cations in $MAPbI_3$ was studied from first-principles calculations. First, we investigated two types of MA cation rotations, including in-phase and out-of-phase rotations, and calculated their energy barriers. Second, the energetic advantage of the FE state relative to the AFE states was determined. Last, we explored means to further enhance the FE dipole ordering. The results can be summarized as below:

(1) The in-phase nonflipping rotation of MA cations is accessible in both cubic and tetragonal phases, while the in-phase flipping rotation is energetically prohibited in the tetragonal phase. The larger the cell aspect ratio c/a is, the less likely MA flipping rotation becomes.
(2) The out-of-phase flipping rotation of MA cations in tetragonal $MAPbI_3$ tends to form FE dipole ordering.
(3) The FE dipole ordering state is energetically more favorable than the AFE states, with a small energetic advantage of 36 meV. Polarization contributed by FE dipole ordering in tetragonal $MAPbI_3$ was calculated to be 3.15 $\mu C/cm^2$.
(4) Based on the change of c/a, compressive strain and substitutional doping with smaller anions can both enhance the energetic advantage of the FE dipole ordering state in tetragonal $MAPbI_3$.

In short, this work reveals the rotational behavior of MA cations and their spontaneous formation of FE dipole ordering in tetragonal $MAPbI_3$ and proposes strain engineering and doping engineering as two approaches to enhancing the tendency of the FE state formation. We feel that this work provides some key insights into design principles of high-efficiency solar cells based on hybrid halide perovskites.

AUTHOR INFORMATION

Corresponding Author

*E-mail: kesong@ucsd.edu. Phone: +1-858-534-2514.

ORCID

Kesong Yang: 0000-0002-9691-0636

Notes

The authors declare no competing financial interest.

ACKNOWLEDGMENTS

K.Y. thanks Dr. Sheng Xu for useful discussions. This work was supported by the Global Research Outreach (GRO) Program of Samsung Advanced Institute of Technology under the award number 20164974 and the National Science Foundation under award number ACI-1550404. This work used the Extreme Science and Engineering Discovery Environment (XSEDE), which is supported by National Science Foundation grant number OCI-1053575.

REFERENCES

(1) Brenner, T. M.; Egger, D. A.; Kronik, L.; Hodes, G.; Cahen, D. Hybrid Organic-inorganic Perovskites: Low-Cost Semiconductors with Intriguing Charge-Transport Properties. *Nat. Rev. Mater.* **2016**, *1*, 15007.
(2) Stranks, S. D.; Snaith, H. J. Metal-Halide Perovskites for Photovoltaic and Light-Emitting Devices. *Nat. Nanotechnol.* **2015**, *10*, 391−402.
(3) NREL, Research Cell Efficiency Records. http://www.nrel.gov/pv/assets/images/efficiency_chart.jpg. Accessed 12 October, 2017.
(4) Burschka, J.; Pellet, N.; Moon, S.-J.; Humphry-Baker, R.; Gao, P.; Nazeeruddin, M. K.; Grätzel, M. Sequential Deposition as a Route to High-Performance Perovskite-Sensitized Solar Cells. *Nature* **2013**, *499*, 316−319.
(5) Etgar, L.; Gao, P.; Xue, Z.; Peng, Q.; Chandiran, A. K.; Liu, B.; Nazeeruddin, M. K.; Grätzel, M. Mesoscopic $CH_3NH_3PbI_3/TiO_2$ Heterojunction Solar Cells. *J. Am. Chem. Soc.* **2012**, *134*, 17396−17399.
(6) Lotsch, B. V. New Light on an Old Story: Perovskites Go Solar. *Angew. Chem., Int. Ed.* **2014**, *53*, 635−637.
(7) Park, N.-G. Organometal Perovskite Light Absorbers Toward a 20% Efficiency Low-Cost Solid-State Mesoscopic Solar Cell. *J. Phys. Chem. Lett.* **2013**, *4*, 2423−2429.
(8) Chen, Q.; De Marco, N.; Yang, Y. M.; Song, T.-B.; Chen, C.-C.; Zhao, H.; Hong, Z.; Zhou, H.; Yang, Y. Under the Spotlight: The Organic-inorganic Hybrid Halide Perovskite for Optoelectronic Applications. *Nano Today* **2015**, *10*, 355−396.
(9) Yamada, Y.; Nakamura, T.; Endo, M.; Wakamiya, A.; Kanemitsu, Y. Near-Band-Edge Optical Responses of Solution-Processed Organic-inorganic Hybrid Perovskite $CH_3NH_3PbI_3$ on Mesoporous TiO_2 Electrodes. *Appl. Phys. Express* **2014**, *7*, 032302.
(10) Foley, B. J.; Marlowe, D. L.; Sun, K.; Saidi, W. A.; Scudiero, L.; Gupta, M. C.; Choi, J. J. Temperature Dependent Energy Levels of Methylammonium Lead Iodide Perovskite. *Appl. Phys. Lett.* **2015**, *106*, 243904.
(11) Snaith, H. J. Perovskites: the Emergence of a New Era for Low-Cost, High-Efficiency Solar Cells. *J. Phys. Chem. Lett.* **2013**, *4*, 3623−3630.
(12) Yin, W.-J.; Shi, T.; Yan, Y. Unique Properties of Halide Perovskites as Possible Origins of the Superior Solar Cell Performance. *Adv. Mater.* **2014**, *26*, 4653−4658.
(13) Buin, A.; Pietsch, P.; Xu, J.; Voznyy, O.; Ip, A. H.; Comin, R.; Sargent, E. H. Materials Processing Routes to Trap-Free Halide Perovskites. *Nano Lett.* **2014**, *14*, 6281−6286.
(14) Dong, Q.; Fang, Y.; Shao, Y.; Mulligan, P.; Qiu, J.; Cao, L.; Huang, J. Electron-Hole Diffusion Lengths > 175 μm in Solution-Grown $CH_3NH_3PbI_3$ Single Crystals. *Science* **2015**, *347*, 967−970.
(15) Shi, D.; Adinolfi, V.; Comin, R.; Yuan, M.; Alarousu, E.; Buin, A.; Chen, Y.; Hoogland, S.; Rothenberger, A.; Katsiev, K.; et al. Low Trap-State Density and Long Carrier Diffusion in Organolead Trihalide Perovskite Single Crystals. *Science* **2015**, *347*, 519−522.
(16) Stranks, S. D.; Eperon, G. E.; Grancini, G.; Menelaou, C.; Alcocer, M. J.; Leijtens, T.; Herz, L. M.; Petrozza, A.; Snaith, H. J. Electron-Hole Diffusion Lengths Exceeding 1 Micrometer in an Organometal Trihalide Perovskite Absorber. *Science* **2013**, *342*, 341−344.
(17) Xing, G.; Mathews, N.; Sun, S.; Lim, S. S.; Lam, Y. M.; Grätzel, M.; Mhaisalkar, S.; Sum, T. C. Long-Range Balanced Electron- and Hole-Transport Lengths in Organic-Inorganic $CH_3NH_3PbI_3$. *Science* **2013**, *342*, 344−347.
(18) Kutes, Y.; Ye, L.; Zhou, Y.; Pang, S.; Huey, B. D.; Padture, N. P. Direct Observation of Ferroelectric Domains in Solution-Processed $CH_3NH_3PbI_3$ Perovskite Thin Films. *J. Phys. Chem. Lett.* **2014**, *5*, 3335−3339.
(19) You, J.; Hong, Z.; Yang, Y. M.; Chen, Q.; Cai, M.; Song, T.-B.; Chen, C.-C.; Lu, S.; Liu, Y.; Zhou, H.; et al. Low-Temperature Solution-Processed Perovskite Solar Cells with High Efficiency and Flexibility. *ACS Nano* **2014**, *8*, 1674−1680.
(20) Zhao, Y.; Zhu, K. Solution Chemistry Engineering Toward High-Efficiency Perovskite Solar Cells. *J. Phys. Chem. Lett.* **2014**, *5*, 4175−4186.
(21) Zhu, H.; Miyata, K.; Fu, Y.; Wang, J.; Joshi, P. P.; Niesner, D.; Williams, K. W.; Jin, S.; Zhu, X.-Y. Screening in Crystalline Liquids Protects Energetic Carriers in Hybrid Perovskites. *Science* **2016**, *353*, 1409−1413.
(22) Zhu, H.; Trinh, M. T.; Wang, J.; Fu, Y.; Joshi, P. P.; Miyata, K.; Jin, S.; Zhu, X.-Y. Organic Cations Might Not Be Essential to the

DOI: 10.1021/acs.jpcc.7b10413
J. Phys. Chem. C 2018, 122, 177−184

Remarkable Properties of Band Edge Carriers in Lead Halide Perovskites. *Adv. Mater.* **2017**, *29*, 1603072.
(23) Miyata, K.; Meggiolaro, D.; Trinh, M. T.; Joshi, P. P.; Mosconi, E.; Jones, S. C.; De Angelis, F.; Zhu, X.-Y. Large Polarons in Lead Halide Perovskites. *Sci. Adv.* **2017**, *3*, e1701217.
(24) Frost, J. M.; Butler, K. T.; Brivio, F.; Hendon, C. H.; Van Schilfgaarde, M.; Walsh, A. Atomistic Origins of High-Performance in Hybrid Halide Perovskite Solar Cells. *Nano Lett.* **2014**, *14*, 2584−2590.
(25) Bi, F.; Markov, S.; Wang, R.; Kwok, Y.; Zhou, W.; Liu, L.; Zheng, X.; Chen, G.; Yam, C. Enhanced Photovoltaic Properties Induced by Ferroelectric Domain Structures in Organometallic Halide Perovskites. *J. Phys. Chem. C* **2017**, *121*, 11151−11158.
(26) Rakita, Y.; Bar-Elli, O.; Meirzadeh, E.; Kaslasi, H.; Peleg, Y.; Hodes, G.; Lubomirsky, I.; Oron, D.; Ehre, D.; Cahen, D. Tetragonal $CH_3NH_3PbI_3$ Is Ferroelectric. *Proc. Natl. Acad. Sci. U. S. A.* **2017**, *114*, E5504−E5512.
(27) Tong, C.-J.; Geng, W.; Prezhdo, O. V.; Liu, L.-M. Role of Methylammonium Orientation in Ion Diffusion and Current-Voltage Hysteresis in the $CH_3NH_3PbI_3$ Perovskite. *ACS Energy Lett.* **2017**, *2*, 1997−2004.
(28) Jankowska, J.; Prezhdo, O. V. Ferroelectric Alignment of Organic Cations Inhibits Nonradiative Electron−Hole Recombination in Hybrid Perovskites: Ab Initio Nonadiabatic Molecular Dynamics. *J. Phys. Chem. Lett.* **2017**, *8*, 812−818.
(29) Kanno, S.; Imamura, Y.; Saeki, A.; Hada, M. Rotational Energy Barriers and Relaxation Times of the Organic Cation in Cubic Methylammonium Lead/Tin Halide Perovskites from First Principles. *J. Phys. Chem. C* **2017**, *121*, 14051−14059.
(30) Stroppa, A.; Quarti, C.; De Angelis, F.; Picozzi, S. Ferroelectric Polarization of $CH_3NH_3PbI_3$: a Detailed Study Based on Density Functional Theory and Symmetry Mode Analysis. *J. Phys. Chem. Lett.* **2015**, *6*, 2223−2231.
(31) Zheng, F.; Takenaka, H.; Wang, F.; Koocher, N. Z.; Rappe, A. M. First-Principles Calculation of the Bulk Photovoltaic Effect in $CH_3NH_3PbI_3$ and $CH_3NH_3PbI_{3-x}Cl_x$. *J. Phys. Chem. Lett.* **2015**, *6*, 31−37.
(32) Fan, Z.; Xiao, J.; Sun, K.; Chen, L.; Hu, Y.; Ouyang, J.; Ong, K. P.; Zeng, K.; Wang, J. Ferroelectricity of $CH_3NH_3PbI_3$ Perovskite. *J. Phys. Chem. Lett.* **2015**, *6*, 1155−1161.
(33) Kim, H.-S.; Kim, S. K.; Kim, B. J.; Shin, K.-S.; Gupta, M. K.; Jung, H. S.; Kim, S.-W.; Park, N.-G. Ferroelectric Polarization in $CH_3NH_3PbI_3$ Perovskite. *J. Phys. Chem. Lett.* **2015**, *6*, 1729−1735.
(34) Weller, M. T.; Weber, O. J.; Henry, P. F.; Di Pumpo, A. M.; Hansen, T. C. Complete Structure and Cation Orientation in the Perovskite Photovoltaic Methylammonium Lead Iodide between 100 and 352 K. *Chem. Commun.* **2015**, *51*, 4180−4183.
(35) Sharada, G.; Mahale, P.; Kore, B. P.; Mukherjee, S.; Pavan, M. S.; De, C.; Ghara, S.; Sundaresan, A.; Pandey, A.; Row, T. N. G.; et al. Is $CH_3NH_3PbI_3$ Polar? *J. Phys. Chem. Lett.* **2016**, *7*, 2412−2419.
(36) Rakita, Y.; Meirzadeh, E.; Bendikov, T.; Kalchenko, V.; Lubomirsky, I.; Hodes, G.; Ehre, D.; Cahen, D. $CH_3NH_3PbBr_3$ Is Not Pyroelectric, Excluding Ferroelectric-Enhanced Photovoltaic Performance. *APL Mater.* **2016**, *4*, 051101.
(37) Kresse, G.; Furthmüller, J. Efficient Iterative Schemes for *Ab-Initio* Total-Energy Calculations Using a Plane-Wave Basis Set. *Phys. Rev. B: Condens. Matter Mater. Phys.* **1996**, *54*, 11169−11186.
(38) Kresse, G.; Furthmüller, J. Efficiency of *Ab-Initio* Total Energy Calculations for Metals and Semiconductors Using a Plane-Wave Basis Set. *Comput. Mater. Sci.* **1996**, *6*, 15−50.
(39) Blöchl, P. Projector Augmented-Wave Method. *Phys. Rev. B: Condens. Matter Mater. Phys.* **1994**, *50*, 17953−17979.
(40) Perdew, J. P.; Burke, K.; Ernzerhof, M. Generalized Gradient Approximation Made Simple. *Phys. Rev. Lett.* **1996**, *77*, 3865−3868.
(41) Stoumpos, C. C.; Malliakas, C. D.; Kanatzidis, M. G. Semiconducting Tin and Lead Iodide Perovskites with Organic Cations: Phase Transitions, High Mobilities, and Near-Infrared Photoluminescent Properties. *Inorg. Chem.* **2013**, *52*, 9019−9038.
(42) Yin, W.-J.; Yan, Y.; Wei, S.-H. Anomalous Alloy Properties in Mixed Halide Perovskites. *J. Phys. Chem. Lett.* **2014**, *5*, 3625−3631.
(43) Momma, K.; Izumi, F. VESTA 3 for Three-Dimensional Visualization of Crystal, Volumetric and Morphology Data. *J. Appl. Crystallogr.* **2011**, *44*, 1272−1276.
(44) Nazir, S.; Behtash, M.; Yang, K. Enhancing Interfacial Conductivity and Spatial Charge Confinement of $LaAlO_3/SrTiO_3$ Heterostructures via Strain Engineering. *Appl. Phys. Lett.* **2014**, *105*, 141602−141605.
(45) Yang, K.; Setyawan, W.; Wang, S.; Nardelli, M. B.; Curtarolo, S. A Search Model for Topological Insulators with High-Throughput Robustness Descriptors. *Nat. Mater.* **2012**, *11*, 614−619.
(46) Jacobsson, T. J.; Correa-Baena, J.-P.; Pazoki, M.; Saliba, M.; Schenk, K.; Grätzel, M.; Hagfeldt, A. Exploration of the Compositional Space for Mixed Lead Halogen Perovskites for High Efficiency Solar Cells. *Energy Environ. Sci.* **2016**, *9*, 1706−1724.
(47) Yan, W.-L.; Lu, G.-H.; Liu, F. Effect of Chlorine Substitution on Lattice Distortion and Ferroelectricity of $CH_3NH_3PbI_3$. *J. Phys. Chem. C* **2016**, *120*, 17972−17977.
(48) Atourki, L.; Vega, E.; Marí, B.; Mollar, M.; Ahsaine, H. A.; Bouabid, K.; Ihlal, A. Role of the Chemical Substitution on the Structural and Luminescence Properties of the Mixed Halide Perovskite Thin $MAPbI_{3-x}Br_x (0 \leq x \leq 1)$ Films. *Appl. Surf. Sci.* **2016**, *371*, 112−117.
(49) Quarti, C.; Mosconi, E.; Umari, P.; De Angelis, F. Chlorine Incorporation in the $CH_3NH_3PbI_3$ Perovskite: Small Concentration, Big Effect. *Inorg. Chem.* **2017**, *56*, 74−83.
(50) Liu, J.; Prezhdo, O. V. Chlorine Doping Reduces Electron−hole Recombination in Lead Iodide Perovskites: Time-Domain Ab Initio Analysis. *J. Phys. Chem. Lett.* **2015**, *6*, 4463−4469.
(51) Jiang, M.; Wu, J.; Lan, F.; Tao, Q.; Gao, D.; Li, G. Enhancing the Performance of Planar Organo-Lead Halide Perovskite Solar Cells by Using a Mixed Halide Source. *J. Mater. Chem. A* **2015**, *3*, 963−967.
(52) Kim, M.-c.; Kim, B. J.; Son, D.-Y.; Park, N.-G.; Jung, H. S.; Choi, M. Observation of Enhanced Hole Extraction in Br Concentration Gradient Perovskite Materials. *Nano Lett.* **2016**, *16*, 5756−5763.
(53) Bi, D.; Tress, W.; Dar, M. I.; Gao, P.; Luo, J.; Renevier, C.; Schenk, K.; Abate, A.; Giordano, F.; Baena, J.-P. C.; et al. Efficient Luminescent Solar Cells Based on Tailored Mixed-Cation Perovskites. *Sci. Adv.* **2016**, *2*, e1501170.

DOI: 10.1021/acs.jpcc.7b10413
J. Phys. Chem. C 2018, 122, 177−184